

Shape dependence of Edelstein and magnetoelectric effects in the \sphericalangle -shaped model

Shuhei Kanda  and Satoru Hayami 

Graduate School of Science, Hokkaido University, Sapporo 060-0810, Japan

(Dated: November 19, 2025)

We theoretically investigate the shape dependence and microscopic mechanism of the magnetoelectric effect, including both nonmagnetic (Edelstein-type) and magnetic origins, in a V-shaped one-dimensional chain model. Numerical calculations based on the Kubo formula reveal that the magnitude of the nonmagnetic-driven magnetoelectric response reaches a maximum at an apex angle of $\theta \approx 0.6\pi$. To clarify the microscopic origin of this behavior, we construct a low-energy effective Hamiltonian by projecting onto the s -orbital subspace and demonstrate that the polarity induced by the V-shaped geometry manifests as an effective spin-orbit interaction. An analytical derivation of the Green's function shows that the geometric effect appears as a T -matrix contribution, reflecting the local breaking of translational symmetry at the V-shaped edge. Furthermore, by employing a multipole-basis representation, we identify the selection rules that govern the magnetoelectric tensor and reveal that the coupling between the effective spin-orbit interaction and the orbital angular momentum generated across the apex plays an essential role. The resulting angular dependence, $\sin\theta \sin\theta/2$, peaks at $\theta = 2 \tan^{-1} \sqrt{2} \approx 0.608\pi$, in good agreement with the numerical results. We also analyze a ferromagnetic V-shaped model including the Zeeman interaction and show that the magnetic-driven magnetoelectric response originates from the spin magnetization induced by the coupling between the electric-field-driven charge-potential gradient and the Zeeman term. These findings demonstrate that the V-shaped geometry gives rise to distinct magnetoelectric mechanisms depending on the presence or absence of time-reversal symmetry and provide a microscopic framework for understanding shape-induced multipole phenomena in mesoscopic and bulk systems.

I. INTRODUCTION

Artificially structured metamaterials (or metasurfaces) have enabled unprecedented creation and manipulation of physical phenomena [1–5]. In particular, recent advances in microfabrication techniques have made it possible to induce specific symmetries into a system, for example, by fabricating holes of designed shapes [6, 7] or by constructing tailored nanostructured architectures [2, 8–11]. Such artificial systems provide a valuable platform for exploring and realizing exotic physical phenomena, which can be flexibly engineered through the geometric parameters of the constituent nanostructures, including their composition, shape, periodicity, and mutual arrangement.

To systematically characterize the symmetry and associated physical responses of such artificially engineered systems, it is essential to adopt a unified theoretical framework. The finite multipole moments in a system reflect its underlying symmetry. The multipole description provides a powerful way to connect macroscopic phenomena, microscopic degrees of freedom, and symmetry principles [12–18]. Microscopic internal degrees of freedom, such as spin, orbital, and charge, can be systematically classified within the multipole basis, which provides a complete set for describing an arbitrary electronic states in a given Hilbert space [12, 16, 18, 19]. Consequently, extensive studies have been devoted to macroscopic response phenomena originating from bulk electronic degrees of freedom using multipole basis. These efforts have employed the multipole basis to extract key model parameters and to characterize the resulting emergent behaviors [17, 18, 20].

Meanwhile, the detailed correspondence between the symmetries induced by mesoscopic geometries and the multipole degrees of freedom remains elusive, except for the level of macroscopic symmetry [13, 15, 18]. For example, it is still unclear how boundary conditions imposed by specific geometries couple to multipole moments and, through what microscopic mechanisms, influence macroscopic physical properties. Elucidating the interplay between geometry-induced metamaterial properties and multipole degrees of freedom provides critical insights into the analysis and design of advanced metamaterial functionalities.

We focus on a V-shaped (so-called “ku-noji”-shaped in Japanese) metamaterial [21–23]. The V-shaped structure possesses C_{2v} ($m2m$) symmetry or C_2 (m) symmetry when the substrate is taken into account. In such metamaterials, the shape-induced polarity gives rise to a finite electric dipole moment, which becomes the microscopic origin of the Edelstein effect [24–27], the nonlinear Hall effect [17, 28–31], the nonlinear optical response [32–35], and the piezoelectric effect [36–38]. Furthermore, in ferromagnetic V-shaped systems, magnetic dipole degrees of freedom originating from spontaneous magnetization become active, leading to a multiferroic state that simultaneously breaks time-reversal and spatial-inversion symmetries. In such multiferroics, magnetic toroidal dipole degrees of freedom, which is characterized by polar vectors that are odd under time-reversal symmetry [12, 18, 39, 40], play an essential role. These toroidal moments give rise to rich physical phenomena such as magnetoelectric (ME) effects [39, 41–47], nonreciprocal conductivity [46, 48–50], and nonreciprocal directional dichroism [11, 51–53].

In this paper, we investigate the shape dependence and the underlying mechanism of the ME response arising from the V-shaped geometry using a one-dimensional (1D) chain model; hereafter, the term ‘‘ME effect’’ is used in a generalized sense to refer collectively to the nonmagnetic-driven Edelstein effect associated with electric dipoles and the magnetic-driven ME response induced by magnetic toroidal dipoles. First, we evaluate the shape dependence of the nonmagnetic-driven ME effect in a model including s and p orbitals. We find that the magnitude of the ME effect reaches its maximum at an apex angle of $\theta \approx 0.6\pi$. To analyze the mechanism underlying this dependence, we next perform a more detailed model analysis. By projecting onto the s -orbital basis, we construct a low-energy effective Hamiltonian, in which the polarity induced by the V-shaped geometry emerges as an effective spin-orbit interaction. Furthermore, by analyzing the shape dependence of the Green’s function, we clarify that the geometric effect manifests itself as a T -matrix contribution to the Green’s function. We then analyzed the selection rules using the multipole basis, which reveals that the effective spin-orbit interaction and the orbital angular momentum generated by motion across the apex angle play essential roles in the ME effect. The angular dependence of this mechanism takes the form $\sin\theta\sin\theta/2$, exhibiting a peak around $\theta = 2\tan^{-1}\sqrt{2} \approx 0.608\pi$, indicating that the shape dependence originates from the underlying mechanism of the ME effect. Finally, we investigate a V-shaped ferromagnetic model including Zeeman interaction. We find that the magnetic-driven ME effect in this case arises from spin magnetization induced by the coupling between the charge-potential gradient generated by the V-shaped geometry and the Zeeman interaction. These distinct physical mechanisms result in different dependence of the ME effect on both shape and system size.

The organization of this paper is as follows. In Sec. II, we present the numerical results demonstrating the shape dependence of the nonmagnetic-driven ME effect in a model including s and p orbitals. In Sec. III, we derive an effective Hamiltonian and show that the polarity induced by the V-shaped geometry results in the effective spin-orbit interaction. In Sec. IV, we analyze the shape dependence of the Green’s function and employ the multipole basis to analyze the selection rules for the ME tensor, thereby clarifying the key physical mechanisms underlying the shape dependence. In Sec. V, we further investigate the shape dependence and the underlying mechanism of the magnetic-driven ME effect in a ferromagnetic system without the time-reversal symmetry. Section VI is devoted to the summary of the present findings. Appendices include the derivation of the Green’s function of the straight 1D chain in Appendix A, the matrix representation of multipoles in the V-shaped model in Appendix B, and the expression of the ME tensor based on the multipole basis in Appendix C.

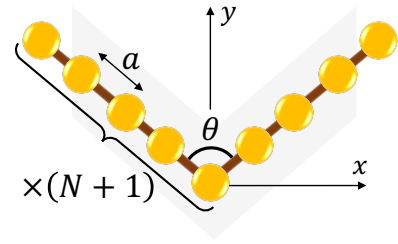


FIG. 1. The lattice of the $2N + 1$ -site ($N = 4$) V-shaped 1D chain defined in Eq. (2). a is the lattice constant and θ is the apex angle.

II. SP-MODEL

We evaluate the shape dependence of the ME effect in a model including s and p orbitals. In Sec. II A, we introduce the s - p -orbital model in the V-shaped chain system. We also show the expression of the linear ME tensor, which describes the correlation between the electric polarization and the magnetization in Sec. II B.

A. Model and Method

We consider a toy model with s and p orbitals in the V-shaped finite chain lying on the xy plane, as shown in Fig. 1. The tight-binding Hamiltonian is given by

$$\hat{H} = \sum_{\mathbf{R}_n \mathbf{R}_{n'}} \sum_{mm'\sigma\sigma'} \hat{\varphi}_{m\sigma}^\dagger(\mathbf{R}_n) \bar{h}_{mm'\sigma\sigma'}^{nn'} \hat{\varphi}_{m'\sigma'}(\mathbf{R}_{n'}), \quad (1)$$

where $\hat{\varphi}_{m\sigma}(\mathbf{R}_n)$ and $\hat{\varphi}_{m\sigma}^\dagger(\mathbf{R}_n)$ are the fermionic annihilation and creation operators of the s - p orbital $m = s, p_x, p_y, p_z$, the spin $\sigma = \uparrow, \downarrow$, and the position \mathbf{R}_n . The V-shaped 1D chain lattice consists of the $2N + 1$ sites, whose positions are specified by \mathbf{R}_n defined as

$$\mathbf{R}_n = a \left(n \sin \frac{\theta}{2}, |n| \cos \frac{\theta}{2} \right) \quad (-N \leq n \leq N), \quad (2)$$

where a is the lattice constant and θ is the apex angle of the V shape, as shown in Fig. 1.

The Hamiltonian is decomposed into three parts as follows:

$$\hat{H} = \hat{H}_{\text{hop}} + \hat{H}_{\Delta} + \hat{H}_{\text{SOC}}. \quad (3)$$

The first term \hat{H}_{hop} represents the hopping term, which includes the Slater-Koster parameters $t_{ss\sigma}$ and $t_{sp\sigma}$ for the nearest-neighbor hopping [54]. The hopping between the p orbitals is neglected ($t_{pp\sigma} = t_{pp\pi} = 0$) for simplicity. \hat{H}_{hop} is given by

$$\hat{H}_{\text{hop}} = \sum_{\mathbf{R}, \delta} \sum_{mm'\sigma} \bar{\varepsilon}_{\delta, mm'} \hat{\varphi}_{m\sigma}^\dagger(\mathbf{R} + a\delta) \hat{\varphi}_{m'\sigma}(\mathbf{R}), \quad (4)$$

where the lattice number n of \mathbf{R}_n is omitted for notational simplicity (e.g., $\mathbf{R} = \mathbf{R}_n, \boldsymbol{\delta} = \boldsymbol{\delta}_n$). $\boldsymbol{\delta}$ is the direction cosine for the nearest-neighbor sites from \mathbf{R} . The relationship between $\bar{\varepsilon}$ and the Slater-Koster parameters is given by

$$\begin{aligned}\bar{\varepsilon}_{\boldsymbol{\delta},ss} &= -t_{ss\sigma}, \\ \bar{\varepsilon}_{\boldsymbol{\delta},sp_i} &= -\bar{\varepsilon}_{\boldsymbol{\delta},p_i s} = t_{sp\sigma}\delta^i \quad (i = x, y), \\ \bar{\varepsilon}_{\boldsymbol{\delta},mm'} &= 0 \quad (\text{otherwise}).\end{aligned}\quad (5)$$

The second term $\hat{\mathcal{H}}_\Delta$ represents the energy level of the p orbital measured from that of the s orbital, which is expressed as

$$\hat{\mathcal{H}}_\Delta = \Delta_p \sum_{\mathbf{R}} \sum_{m\sigma}^{m=p_x, p_y, p_z} \hat{\varphi}_{m\sigma}^\dagger(\mathbf{R}) \hat{\varphi}_{m\sigma}(\mathbf{R}). \quad (6)$$

The third term $\hat{\mathcal{H}}_{\text{SOC}}$ represents the atomic spin-orbit coupling (SOC) term, which is represented by

$$\hat{\mathcal{H}}_{\text{SOC}} = \frac{2\lambda}{\hbar^2} \sum_{\mathbf{R}} \sum_{mm'\sigma\sigma'} \bar{l}_{mm'} \cdot \bar{s}_{\sigma\sigma'} \hat{\varphi}_{m\sigma}^\dagger(\mathbf{R}) \hat{\varphi}_{m'\sigma'}(\mathbf{R}), \quad (7)$$

where \bar{l} and \bar{s} represent the matrices of the orbital and spin angular momentum operators, respectively. \hbar is the reduced Planck constant. It is noted that the orbital angular momentum operator is defined within the p -orbital subspace.

For the above model, we evaluate the ME tensor by using the linear response theory. The ME tensor $\alpha^{\nu;\rho}$, which corresponds to the coefficient describing the linear response of the magnetization δM^ν to an external electric field E^ρ , is defined as:

$$\delta M^\nu = \sum_{\rho} \alpha^{\nu;\rho} E^\rho. \quad (8)$$

Within the framework of linear response theory, the ME tensor incorporates contributions from the Edelstein effect with the dissipation, which preserves time-reversal symmetry, and from the conventional ME effect without the dissipation, which requires its breaking [13–15, 18]. In the V-shaped model preserving time-reversal symmetry, the point-group symmetry of the system is C_{2v} owing to the emergence of electric polarization along the y direction. This polar symmetry allows a finite $\alpha^{z;x}$ component in two-dimensional systems.

We calculate the linear ME tensor using the Kubo formula:

$$\alpha^{\nu;\rho} = -\frac{1}{V} \sum_{AB} \frac{f(E_A) - f(E_B)}{E_A - E_B + i\hbar\gamma} \bar{M}_{AB}^\nu \bar{P}_{BA}^\rho, \quad (9)$$

where E_A are eigenvalue of Hamiltonian matrix \bar{h} , $f(E)$ is the Fermi distribution function, $V = (2N + 1)a$ is the volume of the system, and $\gamma = 1/\tau$ is the scattering rate, characterized as the inverse of the relaxation time τ under

the relaxation time approximation. \bar{M}_{AB}^ν and \bar{P}_{BA}^ρ are matrix elements of the magnetization and polarization operators for eigenstates A and B , respectively. Their operator expressions are given by

$$\hat{M}^\nu = \frac{\mu_B}{\hbar} \left(\hat{L}^\nu + g\hat{S}^\nu \right), \quad (10)$$

$$\hat{L}^\nu = \sum_{\mathbf{R}} \sum_{mm'\sigma} \bar{l}_{mm'}^\nu \hat{\varphi}_{m\sigma}^\dagger(\mathbf{R}) \hat{\varphi}_{m'\sigma}(\mathbf{R}), \quad (11)$$

$$\hat{S}^\nu = \sum_{\mathbf{R}} \sum_{m\sigma\sigma'} \bar{s}_{\sigma\sigma'}^\nu \hat{\varphi}_{m\sigma}^\dagger(\mathbf{R}) \hat{\varphi}_{m\sigma'}(\mathbf{R}), \quad (12)$$

$$\hat{P}^\rho = e \sum_{\mathbf{R}} \sum_{m\sigma} R^\rho \hat{\varphi}_{m\sigma}^\dagger(\mathbf{R}) \hat{\varphi}_{m\sigma}(\mathbf{R}), \quad (13)$$

where e , μ_B , and g are the elementary charge, the Bohr magneton, and the g factor, respectively.

B. Numerical results

We evaluate the shape dependence of the ME tensor $\alpha^{z;x}$ in the V-shaped s - p model as Eq. (3). In the following numerical calculations in this subsection, we set

$$t_{ss\sigma} = 1, t_{sp\sigma} = 0.7, \Delta_p = 10, \lambda = 0.4, \quad (14)$$

and $N = 128$. We also set $e = \hbar = \mu_B = a = 1$, $g = 2$, $\gamma = 0.05$, and the temperature $T = 0.01$. Since we consider the nonmagnetic system with time-reversal symmetry, the ME response $\alpha^{z;x}$ becomes nonzero only under the finite dissipation.

First, we present the chemical potential μ dependence for various apex angles θ . We focus on the range $-2 \leq \mu \leq 2$, in which the electronic states are primarily characterized by the s orbital owing to the large energy separation Δ_p . As shown in Fig. 2(a), $\alpha^{z;x}$ reaches its maximum around $\mu \approx 1.5$ and its minimum around $\mu \approx -1.45$, independent of the value of θ . The disappearance of $\alpha^{z;x}$ for $\theta = \pi$ is owing to the presence of the spatial inversion symmetry, where the system reduces to the straight 1D chain. Meanwhile, the vanishing of $\alpha^{z;x}$ at $\theta = 0$ implies that a finite opening along the x direction in the V-shaped geometry, which results in the x -directional electric polarization, is essential for the nonmagnetic-driven ME effect.

Figure 2(b) shows the θ dependence of the ME effect at $\mu = 0.5$. The magnitude of the ME response exhibits a nearly monotonic dependence on θ , showing a clear peak at an apex angle of approximately $\theta \approx 0.6\pi$. This behavior is clarified by employing the approach based on an effective model in the subsequent section.

III. EFFECTIVE MODEL

To analyze the underlying physical mechanism of the numerically obtained ME response, we adopt an effective model approach that eliminates redundant degrees

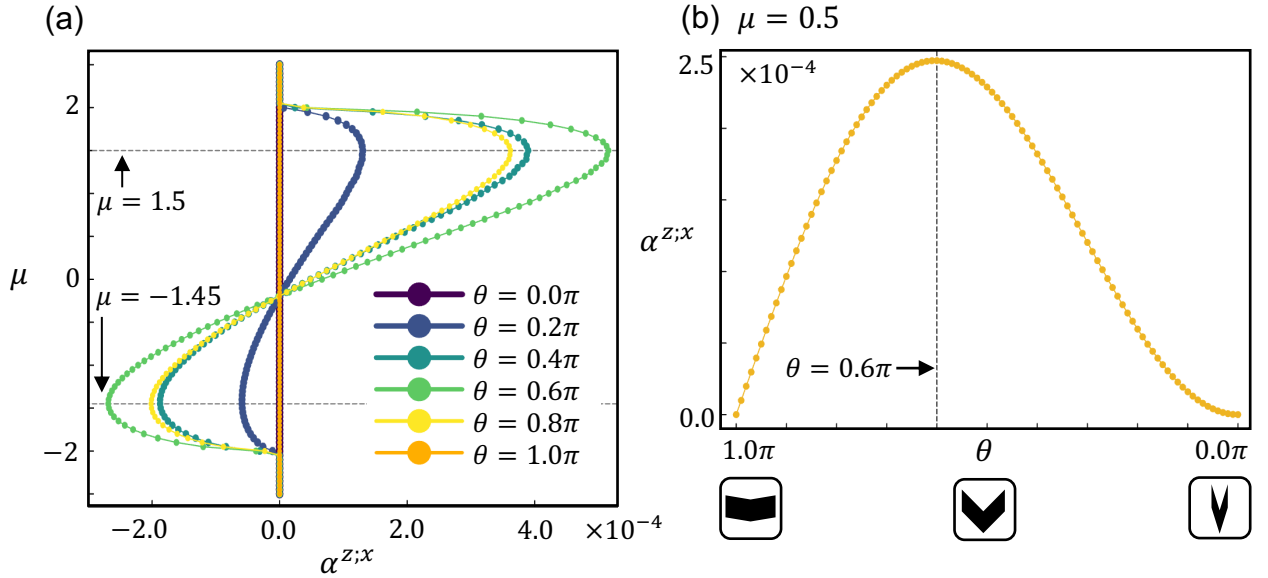


FIG. 2. (a) Chemical potential μ dependence of the nonmagnetic-driven ME tensor component $\alpha^{z;x}$ for various apex angles, $\theta = 0.0\pi, 0.2\pi, \dots, 1.0\pi$. $\alpha^{z;x}$ reaches its maximum around $\mu \approx 1.5$ and its minimum around $\mu \approx -1.45$, independent of the value of θ . (b) Apex angle θ dependence of the ME tensor at $\mu = 0.5$. The magnitude of the ME response induced by the V-shaped geometry reaches its maximum at $\theta \approx 0.6\pi$. In both (a) and (b), the parameters are set to $t_{ss\sigma} = 1, t_{sp\sigma} = 0.7, \Delta_p = 10, \lambda = 0.4, N = 128, \gamma = 0.05$, and $T = 0.01$.

of freedom to capture the essential physics. To this end, we derive an effective Hamiltonian by projecting the s - p orbital model onto the s -orbital subspace [55–58]:

$$\hat{\mathcal{H}}_{\text{eff}}(z) = \sum_{\mathbf{R}_n, \mathbf{R}_{n'}} \sum_{\sigma\sigma'} \hat{\varphi}_{s\sigma}^\dagger(\mathbf{R}_n) [\bar{h}_{\text{eff}}(z)]_{\sigma\sigma'}^{nn'} \hat{\varphi}_{s\sigma'}(\mathbf{R}_{n'}), \quad (15)$$

$$\bar{h}_{\text{eff}}(z) = \bar{P}_s \bar{h} \bar{P}_s + \bar{\eta}^\dagger \bar{g}_\perp(z) \bar{\eta}, \quad (16)$$

where $\bar{g}_\perp(z) = (\hbar z - \bar{Q}_p \bar{h} \bar{Q}_p)^{-1}$, $\bar{\eta} = \bar{Q}_p \bar{h} \bar{P}_s$, \bar{h} is the matrix of the s - p Hamiltonian in Eq. (3), and \bar{P}_s and \bar{Q}_p are the projection operators for s -orbital and p -orbital bases, respectively. The effective Hamiltonian is thereby decomposed into three parts as follows:

$$\hat{\mathcal{H}}_{\text{eff}}(z) = \hat{\mathcal{H}}_{\text{hop}}^{ss\sigma} + \hat{\mathcal{H}}_{\text{hop}}^{2\text{nd}}(z) + \hat{\mathcal{H}}_{\text{SOI}}^{\text{eff}}(z). \quad (17)$$

The first term $\hat{\mathcal{H}}_{\text{hop}}^{ss\sigma}$ represents the nearest-neighbor hopping between s orbitals in Eq. (4). The second term $\hat{\mathcal{H}}_{\text{hop}}^{2\text{nd}}(z)$ represents the 2nd-nearest-neighbor hopping through the s - p hybridization, which is given by

$$\hat{\mathcal{H}}_{\text{hop}}^{2\text{nd}}(z) = \sum_{\mathbf{R}, \delta^i \delta^o} \sum_{\sigma} \varepsilon_{\delta^i \delta^o} \hat{\varphi}_{s\sigma}^\dagger(\mathbf{R} + a\delta^o) \hat{\varphi}_{s\sigma}(\mathbf{R} - a\delta^i), \quad (18)$$

where

$$\varepsilon_{\delta^i \delta^o} = -u(z) (\delta^i \cdot \delta^o), \quad (19a)$$

$$u(z) = \frac{-t_{sp\sigma}^2 (\hbar z - \Delta_p + \lambda)}{(\hbar z - \Delta_p - \lambda)(\hbar z - \Delta_p + 2\lambda)}, \quad (19b)$$

and δ^i and δ^o are the direction cosines to the nearest-neighbor sites of \mathbf{R} .

The third term $\hat{\mathcal{H}}_{\text{SOI}}^{\text{eff}}(z)$ represents the effective spin-orbit interaction, which is also induced by the s - p hybridization as

$$\begin{aligned} \hat{\mathcal{H}}_{\text{SOI}}^{\text{eff}}(z) &= \frac{2\alpha(z)}{\hbar^2} \sum_{\mathbf{R}, \delta^i \delta^o} \sum_{\sigma\sigma'} \mathbf{l}_{\delta^i \delta^o} \cdot \bar{s}_{\sigma\sigma'} \hat{\varphi}_{s\sigma}^\dagger(\mathbf{R} + a\delta^o) \hat{\varphi}_{s\sigma'}(\mathbf{R} - a\delta^i), \end{aligned} \quad (20)$$

where

$$\mathbf{l}_{\delta^i \delta^o} = i\hbar(\delta^i \times \delta^o), \quad (21a)$$

$$\alpha(z) = \frac{t_{sp\sigma}^2 \lambda}{(\hbar z - \Delta_p - \lambda)(\hbar z - \Delta_p + 2\lambda)}. \quad (21b)$$

Effective spin-orbit interaction $\hat{\mathcal{H}}_{\text{SOI}}^{\text{eff}}$ arises from the coupling between the orbital angular momentum generated by two successive $sp\sigma$ hoppings and the on-site atomic spin-orbit coupling in the absence of local spatial inversion symmetry with nonzero $\delta^i \times \delta^o$. Reflecting this, in our effective model, $\mathbf{l}_{\delta^i \delta^o}$ takes a finite value only at the V-shaped edge at $n = 0$ within the nearest-neighbor $sp\sigma$ hopping:

$$\mathbf{l}_{\delta^i \delta^o}^z = \begin{cases} \pm i\hbar \sin \theta & (\delta^i = \mathbf{R}_0 - \mathbf{R}_{\mp 1}, \delta^o = \mathbf{R}_{\pm 1} - \mathbf{R}_0) \\ 0 & (\text{otherwise}) \end{cases}. \quad (22)$$

tensor in Eq. (24) are illustrated by the Feynman diagrams shown in Fig. 3(a-c), respectively. For the bubble diagram confined within the s -orbital subspace, the effects of the s - p hybridization and the magnetic elements defined on the p orbitals are incorporated. As shown in Eq. (26) and Fig. 3(a), by including the s - p hybridization in the Green's function to infinite order with even numbers of hybridization processes, the effective Green's function $\bar{\mathcal{G}}_{\text{eff}}$ is obtained. The Green's function components containing an odd number of s - p hybridizations propagate through another Green's function, which also includes an odd number of hybridizations mediated by the magnetic operator defined on the p -orbitals. Consequently, the effective ME tensor defined in Eq. (24) emerges.

IV. DISCUSSION

A. Shape-induced effects in the Green's function

We evaluate the angular dependence of the Green's function in Eq. (25). The Hamiltonian matrix can be separated into the $\theta = \pi$ component and the remaining contributions as follows:

$$\bar{h}_{\text{eff}} = \bar{h}_{\text{eff}}|_{\theta=\pi} + \Delta\bar{h}_{\text{eff}}^{(\theta)}. \quad (28)$$

In our effective model in Eq. (17), $\Delta\bar{h}_{\text{eff}}^{(\theta)}$ takes a finite value only on the sites adjacent to the apex of the V-shaped 1D chain, as shown in Eq. (22). Therefore, $\Delta\bar{h}_{\text{eff}}^{(\theta)}$ is given by 4×4 matrix:

$$\Delta\bar{h}_{\text{eff}}^{(\theta)}(z) = \begin{pmatrix} 0 & u(z)(1 + \cos\theta)\bar{\sigma}_0 - i\alpha(z)\sin\theta\bar{\sigma}_z \\ (-i \rightarrow i) & 0 \end{pmatrix}, \quad (29)$$

where the matrix representation corresponds to the two sites adjacent to the apex angle of the V-shaped 1D chain, \mathbf{R}_{-1} and \mathbf{R}_{+1} , in Eq. (2). $\bar{\sigma}_0$ and $\bar{\sigma}_\nu$ ($\nu = x, y, z$) are the identity matrix and Pauli matrices for spin, respectively. In this section, $(-i \rightarrow i)$ denotes taking the conjugate transpose without taking the conjugate of the coefficients [e.g., $u(z)$ and $\alpha(z)$]. Here, it corresponds to the other off-diagonal component obtained by replacing $-i$ with i .

Then, using $\Delta\bar{h}_{\text{eff}}^{(\theta)}$, the following Dyson equation is obtained:

$$\bar{\mathcal{G}}_{\text{eff}} = \bar{\mathcal{G}}_{\text{eff}}^{(\pi)} + \bar{\mathcal{G}}_{\text{eff}}^{(\pi)} \Delta\bar{h}_{\text{eff}}^{(\theta)} \bar{\mathcal{G}}_{\text{eff}}, \quad (30)$$

where, $\bar{\mathcal{G}}_{\text{eff}}^{(\pi)} = \bar{\mathcal{G}}_{\text{eff}}|_{\theta=\pi}$. It is noted that when $\theta = \pi$, the V-shaped 1D chain represented by Eq. (2) corresponds to a simple 1D chain with the spatial inversion symmetry. Accordingly, $\bar{\mathcal{G}}_{\text{eff}}^{(\pi)}$ is evaluated analytically, with the detailed derivation presented in Appendix A. Then, by solving Eq. (30), we obtain the following expression:

$$\bar{\mathcal{G}}_{\text{eff}} = \bar{\mathcal{G}}_{\text{eff}}^{(\pi)} + \bar{\mathcal{G}}_{\text{eff}}^{(\pi)} \bar{\mathcal{T}}^{(\theta)} \bar{\mathcal{G}}_{\text{eff}}^{(\pi)}, \quad (31)$$

where $\bar{\mathcal{T}}^{(\theta)}$ is the transition matrix (T -matrix) with respect to the V-shaped geometry:

$$\bar{\mathcal{T}}^{(\theta)}(z) = \Delta\bar{h}_{\text{eff}}^{(\theta)} \frac{1}{1 - \bar{\mathcal{G}}_{\text{eff}}^{(\pi)} \Delta\bar{h}_{\text{eff}}^{(\theta)}}. \quad (32)$$

The shape is characterized by the breaking of translational symmetry at the surface site with $n = 0$ [61]. Consequently, a formal structure analogous to the T -matrix emerges in this case, in close analogy to impurity scattering [62, 63]. Therefore, the T -matrix $\bar{\mathcal{T}}^{(\theta)}$ encodes information about the shape of the Hamiltonian. Moreover, since the T -matrix reflects the local effects of the shape, it can be analyzed within a smaller subspace than the full Hamiltonian, expressed as the $2(2N+1) \times 2(2N+1)$ matrix. In our effective model in Eq. (17), $\bar{\mathcal{T}}^{(\theta)}$ is given by the following 4×4 matrix:

$$\bar{\mathcal{T}}^{(\theta)}(z) = \begin{pmatrix} \mathcal{T}_{q_0^c\sigma_0} & \mathcal{T}_{q_0^b\sigma_0}\bar{\sigma}_0 - i\mathcal{T}_{t_x^b\sigma_z}\bar{\sigma}_z \\ (-i \rightarrow i) & \mathcal{T}_{q_0^c\sigma_0}\bar{\sigma}_0 \end{pmatrix}. \quad (33)$$

$\mathcal{T}_{q_0^c\sigma_0}$, $\mathcal{T}_{q_0^b\sigma_0}$, and $\mathcal{T}_{t_x^b\sigma_z}$ are nonzero components in $\bar{\mathcal{T}}^{(\theta)}$. The subscripts indicate the coefficient of the matrix basis: q_0^c , q_0^b , and t_x^b denote the multipoles defined in the two-site subspace, which will be introduced later in Sec. IV B and Appendix C. Nonzero off-diagonal components over two sites in $\bar{\mathcal{T}}^{(\theta)}$ are mainly determined by $\Delta\bar{h}_{\text{eff}}^{(\theta)}$, which is composed of the 2nd-nearest-neighbor hopping ($\sim q_0^b\sigma_0$) and the effective spin-orbit interaction (product of imaginary hopping and spin $\sim t_x^b\sigma_z$), as shown in Eq. (29). In contrast, the diagonal components are mainly determined by $(\Delta\bar{h}_{\text{eff}}^{(\theta)})^2$ ($\sim q_0^c\sigma_0$).

Similarly to the Hamiltonian matrix in Eq. (28), the angular θ dependence of the effective magnetization is separated as follows:

$$\bar{M}_{\text{eff}}^\nu = \bar{M}_{\text{eff}}^{\nu(\pi)} + \Delta\bar{M}_{\text{eff}}^{\nu(\theta)}, \quad (34)$$

where $\bar{M}_{\text{eff}}^{\nu(\pi)} = \bar{M}_{\text{eff}}^\nu|_{\theta=\pi}$. In our effective model in Eq. (17), $\Delta\bar{M}_{\text{eff}}^{z(\theta)}$ is, like $\bar{\mathcal{T}}^{(\theta)}$, given by the 4×4 matrix as follows:

$$\Delta\bar{M}_{\text{eff}}^{z(\theta)}(z_1, z_2) = \begin{pmatrix} 0 & \Delta M_{q_0^b\sigma_z}\bar{\sigma}_z - i\Delta M_{t_x^b\sigma_0}\bar{\sigma}_0 \\ (-i \rightarrow i) & 0 \end{pmatrix}, \quad (35)$$

where $\Delta M_{q_0^b\sigma_z}$ and $\Delta M_{t_x^b\sigma_0}$ are nonzero components in $\Delta\bar{M}_{\text{eff}}^{z(\theta)}$; $\Delta M_{q_0^b\sigma_z}$ corresponds to the contribution from the spin magnetization, while $\Delta M_{t_x^b\sigma_0}$ corresponds to that from the orbital magnetization. In our model, $\Delta\bar{M}_{\text{eff}}^{z(\theta)}$ is constrained to the form given in Eq. (35) through Eq. (27), analogous to $\Delta\bar{h}_{\text{eff}}^{(\theta)}$ [Eq. (29)].

We evaluate the apex angle θ dependence of $\bar{\mathcal{T}}^{(\theta)}$ and $\Delta\bar{M}_{\text{eff}}^{z(\theta)}$. We set the Hamiltonian parameters given in Eq. (14). We also set the chemical potential $\mu = 0.5$ and the complex frequencies that is an argument of $\bar{\mathcal{T}}^{(\theta)}$ and $\Delta\bar{M}_{\text{eff}}^{z(\theta)}$: $z = z_1 = z_2 = 0.5\pi i$. Figure 4(a) shows the θ

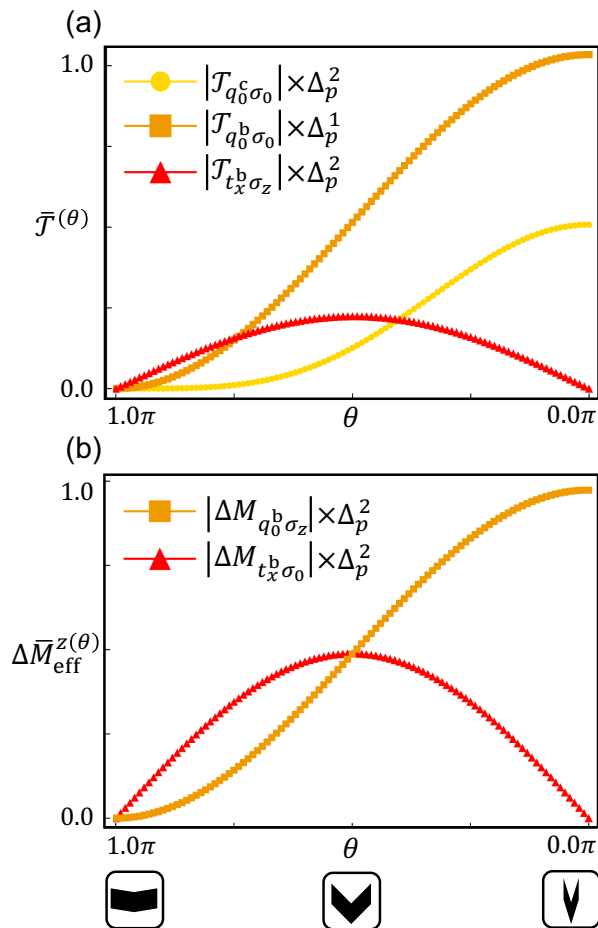


FIG. 4. Absolute values of the components of (a) $\bar{\mathcal{T}}^{(\theta)}$ and (b) $\Delta \bar{M}_{\text{eff}}^{z(\theta)}$ as a function of the apex angle θ . We fix the chemical potential $\mu = 0.5$ and the complex frequencies $z = z_1 = z_2 = 0.5\pi i$, and we use the other model parameters in Eq. (14). In both cases, the terms including q_0^c and q_0^b exhibit a $(1 + \cos\theta)$ -type behavior, whereas that including t_x^b shows a $\sin\theta$ -type dependence. Furthermore, the obtained results display the Δ_p dependence consistent with Eqs. (27) and (37).

dependences of $\bar{\mathcal{T}}^{(\theta)}$, where we find that each coefficient is expressed by the following expressions as

$$\begin{aligned} \mathcal{T}_{q_0^c \sigma_0} &\propto \Delta_p^{-2} (1 + \cos\theta)^2, \\ \mathcal{T}_{q_0^b \sigma_0} &\propto \Delta_p^{-1} (1 + \cos\theta), \\ \mathcal{T}_{t_x^b \sigma_z} &\propto \Delta_p^{-2} \sin\theta. \end{aligned} \quad (36)$$

This dependence is obtained by analyzing the following expression:

$$\bar{\mathcal{T}}^{(\theta)}(z) = \Delta \bar{h}_{\text{eff}}^{(\theta)} + O(\Delta \bar{h}_{\text{eff}}^{(\theta)} \bar{\mathcal{G}}_{\text{eff}}^{(\pi)} \Delta \bar{h}_{\text{eff}}^{(\theta)}) \quad (\Delta_p \rightarrow \infty). \quad (37)$$

Compared to Eq. (29), the off-diagonal components $\mathcal{T}_{q_0^b \sigma_0}$ and $\mathcal{T}_{t_x^b \sigma_z}$ reflect the Δ_p and θ dependence of the 2nd-nearest-neighbor hopping ($u \propto \Delta_p^{-1}$) and the effective

spin-orbit interaction ($\alpha \propto \Delta_p^{-2}$), respectively. Moreover, the diagonal components $\mathcal{T}_{q_0^c \sigma_0}$ arises through the square of the 2nd-nearest-neighbor hopping at the lowest order in Δ_p^{-1} . It is also noted from the above equation in Eq. (37) that when $\bar{\mathcal{G}}_{\text{eff}}^{(\pi)}(z)$ becomes large (for example, when $\text{Im}z$ is sufficiently small and $\text{Re}z$ corresponds to the resonant frequency), this power expansion breaks down, and the θ dependence deviates from Eq. (36).

In the same manner, the θ dependence of $\Delta \bar{M}_{\text{eff}}^{z(\theta)}$ in Fig. 4(b) is given as follows:

$$\begin{aligned} \Delta M_{q_0^b \sigma_z} &\propto \Delta_p^{-2} (1 + \cos\theta), \\ \Delta M_{t_x^b \sigma_0} &\propto \Delta_p^{-2} \sin\theta. \end{aligned} \quad (38)$$

This behavior is understood from Eq. (27); $\bar{g}_{\perp}(z) \propto \Delta_p^{-1} (\Delta_p \gg z)$ at the lowest order in Δ_p^{-1} . $\Delta M_{q_0^b \sigma_z}$ and $\Delta M_{t_x^b \sigma_0}$ arise from the even- and odd-order terms of the angular momentum operator \bar{l}^z , as given in Eqs. (19) and (21), respectively. Therefore, the resulting θ dependence is analogous to that of $\Delta \bar{h}_{\text{eff}}^{(\theta)}$ shown in Eq. (29). Furthermore, because the angular dependence originates solely from $\bar{\eta}$, no θ dependence appears in the denominator term; consequently, Eq. (38) appears as a direct proportional relation, unlike $\bar{\mathcal{T}}^{(\theta)}$.

B. Selection rules using multipole representation

Finally, we introduce the multipole basis and clarify the underlying mechanism by taking into account the selection rules. By employing the symmetry-adapted multipole basis [17, 18, 20, 64–66], arbitrary operators such as the effective Hamiltonian can be expanded by the products of the cluster and bond degrees of freedom (denoted as cluster multipole and bond multipole, respectively) and the spin degree of freedom.

Table I summarizes the multipole degrees of freedom included in each operator in our effective model. The onsite degrees of freedom are described by the cluster electric multipole \bar{q}^c , while the off-site degrees of freedom are described by the bond electric multipole \bar{q}^{bn} and the bond magnetic toroidal multipole \bar{t}^{bn} ; the former (latter) corresponds to the real (imaginary) hopping. Here, the superscript n denotes the bond between the n th nearest-neighbor sites, and the prime ($'$) indicates the quantity defined only on the two sites adjacent to the apex angle (\mathbf{R}_{-1} and \mathbf{R}_{+1}) of the V-shaped 1D chain. The spin degrees of freedom are represented by the Pauli matrices: $\bar{\sigma}_0$ corresponds to the electric monopole, while $(\bar{\sigma}_x, \bar{\sigma}_y, \bar{\sigma}_z)$ represents the magnetic dipole. The matrix representations of the relevant multipoles are given in Appendix B.

Table I presents the dependence on the apex angle θ and the s - p energy separation Δ_p for $\Delta_p \rightarrow \infty$. The simple 1D chain Green's function $\bar{\mathcal{G}}_{\text{eff}}^{(\pi)}$ includes all cluster and bond multipoles generated by arbitrary powers of the hopping Hamiltonian. The simple 1D chain effective

TABLE I. List of multipoles included in the representative operators related to the ME tensor. For simplicity, notations such as “-” are omitted (e.g., $\mathcal{G}^{(\pi)} = \bar{\mathcal{G}}_{\text{eff}}^{(\pi)}$). In the multipole notation, the superscripts c and b denote cluster and bond multipoles, the superscript n following b denotes the n th nearest neighbor, the subscripts 0 and (x, y) denote the monopole and dipole, respectively, and the prime (') indicates the quantity defined on the two sites adjacent to the apex angle (\mathbf{R}_{-1} and \mathbf{R}_{+1}) of the V-shaped 1D chain. For $\bar{M}_{\text{eff}}^{z(\pi)}$, the edge correction due to the 2nd-nearest-neighbor hopping to the onsite term is not taken into account. In the second column, the corresponding irreducible representations (IRs) under the point group C_{2v} are shown, where the superscript \pm denotes the parity with respect to the time-reversal operation. In the last column, the dependence on the apex angle θ and the s - p energy separation Δ_p ($\Delta_p \rightarrow \infty$) is shown.

Operator	IR	Relevant Multipole	θ, Δ_p dep.
$\mathcal{G}^{(\pi)}$	A_1^+	$q_0^c \sigma_0, q_0^{b1} \sigma_0, q_0^{b2} \sigma_0, \dots$	$\propto 1$
$M^{z(\pi)}$	B_1^-	$q_0^c \sigma_z$ $q_0^{b2} \sigma_z$	$\propto 1$ $\propto \Delta_p^{-2}$
$\mathcal{T}^{(\theta)}$	A_1^+	$q_0^c \sigma_0$ $q_0^{b2'} \sigma_0$ $t_x^{b2'} \sigma_z$	$\sim \Delta_p^{-2} (1 + \cos \theta)^2$ $\sim \Delta_p^{-1} (1 + \cos \theta)$ $\sim \Delta_p^{-2} \sin \theta$
$\Delta M^{z(\theta)}$	B_1^-	$q_0^{b2'} \sigma_z$ $t_x^{b2'} \sigma_0$	$\propto \Delta_p^{-2} (1 + \cos \theta)$ $\propto \Delta_p^{-2} \sin \theta$
P^x	B_1^+	$q_x^c \sigma_0$	$\propto \sin \theta / 2$
P^y	A_1^+	$q_y^c \sigma_0$	$\propto \cos \theta / 2$

magnetization $\bar{M}_{\text{eff}}^{z(\pi)}$ contains $\bar{q}_0^c \bar{\sigma}_z$ component and also has $\bar{q}_0^{b2} \bar{\sigma}_z$ component associated with the 2nd-nearest-neighbor hopping. Both originate from the spin magnetization contribution. $\bar{\mathcal{T}}^{(\theta)}$ and $\Delta \bar{M}_{\text{eff}}^{z(\theta)}$ are discussed in Sec. IV A. It is noteworthy that, once the effective magnetization is introduced, the magnetic dipole operator is no longer a pure magnetic dipole but acquires an admixture of the magnetic toroidal dipole $\bar{t}_x^{b2'} \bar{\sigma}_0$. Although the magnetic dipole and the magnetic toroidal dipole are distinct multipoles, they belong to the same irreducible representation in the present system. The multipole $\bar{t}_x^{b2'} \bar{\sigma}_0$ arises from the coupling between the orbital magnetization and the $sp\sigma$ hopping. Finally, the θ dependence of \bar{P}^x and \bar{P}^y is given from Eq. (2).

In order for the ME tensor defined in Eq. (24) to acquire a finite value, the condition $\text{Tr}[*] \neq 0$ must be satisfied. Within the framework of the multipole basis, the following relations play a key role:

$$\bar{q}_0^{b2'} \bar{t}_x^{b2'} \bar{q}_x^c = -i \bar{q}_0^c, \quad (39a)$$

$$\bar{\sigma}_z \bar{\sigma}_z = \bar{\sigma}_0. \quad (39b)$$

By taking into account the above processes and extracting the contributions that satisfy Eq. (39) while retaining only the terms in powers of Δ_p^{-1} , the dominant contribu-

tions can be expressed as

$$\alpha_{\text{eff}}^{z;x} (i\omega_m) = \alpha_i^{z;x} + \alpha_{\text{ii}}^{z;x} + \alpha_{\text{iii}}^{z;x} + \alpha_{\text{iv}}^{z;x} + O(\Delta_p^{-4}) \quad (40)$$

The corresponding diagrams are schematically shown in Fig. 5. The detailed calculations and the explicit expressions are provided in Appendix C. From Table I, the θ and Δ_p dependence of $\alpha_i^{z;x}$, $\alpha_{\text{ii}}^{z;x}$, $\alpha_{\text{iii}}^{z;x}$, and $\alpha_{\text{iv}}^{z;x}$ is given as follows:

$$\alpha_i^{z;x} \propto \Delta_p^{-2} \sin \theta \sin \frac{\theta}{2}, \quad (41a)$$

$$\alpha_{\text{ii}}^{z;x} \sim \Delta_p^{-3} (1 + \cos \theta) \sin \theta \sin \frac{\theta}{2}, \quad (41b)$$

$$\alpha_{\text{iii}}^{z;x} \sim \Delta_p^{-2} \sin \theta \sin \frac{\theta}{2}, \quad (41c)$$

$$\alpha_{\text{iv}}^{z;x} \sim \Delta_p^{-3} (1 + \cos \theta) \sin \theta \sin \frac{\theta}{2}. \quad (41d)$$

As illustrated in Fig. 5, the ME response in our model arises from two distinct processes. The components $\alpha_i^{z;x}$ and $\alpha_{\text{ii}}^{z;x}$ are represented by the coupling among the polarization ($P_{q_x^c \sigma_0}$) and the magnetization ($\Delta M_{t_x^{b2'} \sigma_0}$) through the hopping across the apex angle ($\bar{q}_0^{b2} \bar{\sigma}_0$) in the Green's function, where $P_{q_x^c \sigma_0}$ and $\Delta M_{t_x^{b2'} \sigma_0}$ represent the charge-potential gradient induced by the applied electric field and the orbital magnetization, respectively. Thus, $\alpha_i^{z;x}$ ($\alpha_{\text{ii}}^{z;x}$) represents the (higher-order) contributions arising from the coupling between charge-potential gradient and the orbital magnetization. In contrast, the components $\alpha_{\text{iii}}^{z;x}$ and $\alpha_{\text{iv}}^{z;x}$ are represented by the coupling among the polarization ($P_{q_x^c \sigma_0}$), the spin magnetization ($M_{q_0^c \sigma_z}$), and the spin-dependent hopping across the apex angle in the T -matrix ($\bar{t}_x^{b2'} \bar{\sigma}_z$). Since $\bar{t}_x^{b2'} \bar{\sigma}_z$ represents the contribution from the effective spin-orbit interaction [Eq. (37)], $\alpha_{\text{iii}}^{z;x}$ ($\alpha_{\text{iv}}^{z;x}$) is interpreted as the (higher-order) couplings between the charge-potential gradient and spin magnetizations via the effective spin-orbit interaction.

Figure 6 shows the θ dependence of the components $\alpha_i^{z;x}$, $\alpha_{\text{ii}}^{z;x}$, $\alpha_{\text{iii}}^{z;x}$, and $\alpha_{\text{iv}}^{z;x}$ at the chemical potential $\mu = 0.5$, where we use the same model parameters as those in Fig. 2(a) except for the bosonic Matsubara frequency $\gamma = \omega_1 = 0.02\pi$. We also present their total contribution and the result calculated by using the Kubo formula [Eq. (9)] in the original s - p model. It is demonstrated that the summation of the above four components successfully reproduces the result obtained from the s - p model, indicating the dominant contributions are given by $\alpha_i^{z;x} - \alpha_{\text{iv}}^{z;x}$. Among them, we find that the contribution from $\alpha_i^{z;x}$ is the most dominant, and thereby, the θ dependence of the total $\alpha_{\text{eff}}^{z;x}$ is governed as

$$\alpha_{\text{eff}}^{z;x} \propto \sin \theta \sin \frac{\theta}{2}. \quad (42)$$

This behavior arises from the competition between the maximization of the orbital angular momentum at the angle of the V shape ($\propto \sin \theta$) and the gain in the charge-potential gradient induced by the electric field

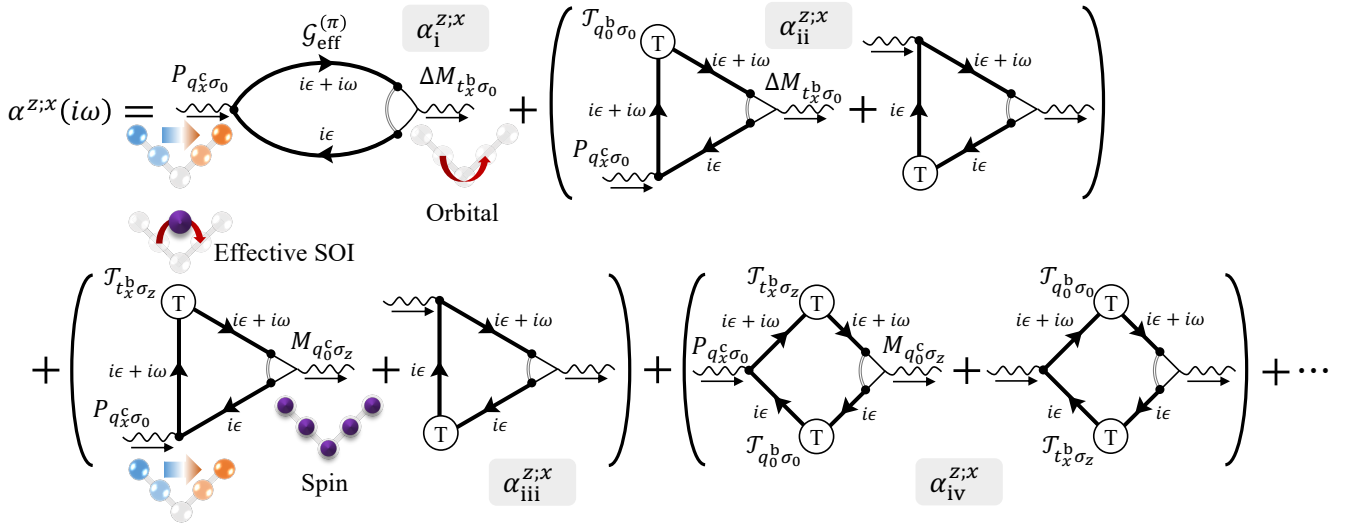


FIG. 5. Diagrams representing distinct processes for the ME effect in our effective models. The thick black line represents the simple 1D chain Green's function at $\theta = \pi$, and the circled T (\textcircled{T}) represents the T -matrix about the V shape in Eq. (32). The subscripts of the Matsubara frequencies are omitted. The symbols (e.g., $P_{q_x^c \sigma_0}$) attached to the operators correspond to their multipole components in Table I. The physical mechanisms corresponding to each multipole component are shown along with their schematic illustrations (see also Fig. 8 in Appendix B). There are two primary physical mechanisms contributing to the ME effect: One is the coupling between the charge-potential gradient induced by the incident electric field and the orbital magnetization ($\alpha_i^{z;x}$ and $\alpha_{ii}^{z;x}$). The other is the spin magnetizations induced by the electric field through the effective spin-orbit interaction ($\alpha_{iii}^{z;x}$ and $\alpha_{iv}^{z;x}$).

along the x direction ($\propto \sin \theta/2$). It exhibits a peak at $\theta = 2 \tan^{-1} \sqrt{2} \approx 0.608\pi$, which is consistent with the result in Fig. 2(b).

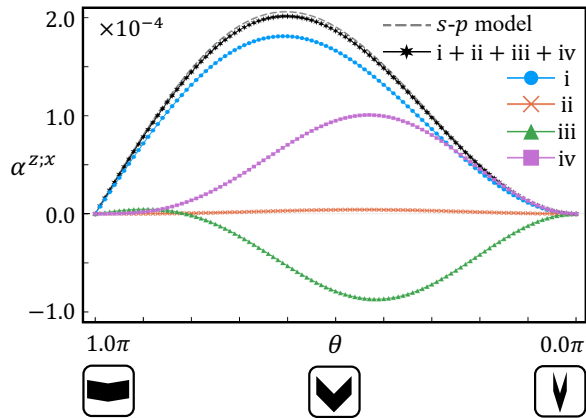


FIG. 6. Apex angle θ dependence of the components of the effective ME tensor $\alpha_i^{z;x}$, $\alpha_{ii}^{z;x}$, $\alpha_{iii}^{z;x}$, and $\alpha_{iv}^{z;x}$. We also present their total contribution and the result calculated using the Kubo formula [Eq. (9)] in the s - p model. We set the Hamiltonian parameters as Eq. (14), and $N = 128$, $\mu = 0.5$, and $T = 0.01$. We also set the scattering rate and the bosonic Matsubara frequency $\gamma = \omega_1 = 0.02\pi$.

V. FERROMAGNETIC SYSTEM

In this section, we consider the effect of the time-reversal-symmetry breaking by additionally taking into account the ferromagnetic mean field along the z direction. For that purpose, we include a Zeeman interaction in the Hamiltonian:

$$\hat{\mathcal{H}}_{Zee} = \frac{b}{\hbar} (\hat{L}^z + g\hat{S}^z). \quad (43)$$

The introduction of a ferromagnetic moment along the z direction induces a magnetic toroidal dipole T_x along the x direction through its coupling to the electric polarization along the y direction, which arises from the V-shaped geometry. Consequently, from the viewpoint of symmetry, the ME response driven by the magnetic toroidal dipole, i.e., the magnetic-driven ME, is induced in the $\alpha^{z;y}$ component [13, 15, 18].

We investigate the shape dependence of the isothermal ME tensor $\alpha_T^{z;y} = \alpha^{z;y}|_{\gamma=0}$ in the V-shaped s - p model. Figure 7(a) shows the θ dependence of the isothermal ME response. We use the Hamiltonian parameters in Eq. (14) and $b = 0.3$; the other parameters are set to $N = 128$, $\mu = 2$, and $T = 0.01$. In contrast to the previous results of nonmagnetic-driven $\alpha^{z;x}$, the magnitude increases monotonically as the apex angle θ decreases.

In the magnetic-driven ME response, the underlying mechanism is more straightforward than that of the nonmagnetic-driven $\alpha^{z;x}$, since the Zeeman interaction introduces an additional component into $\bar{\mathcal{G}}^{(\pi)}$ as $q_0^c \sigma_z$,

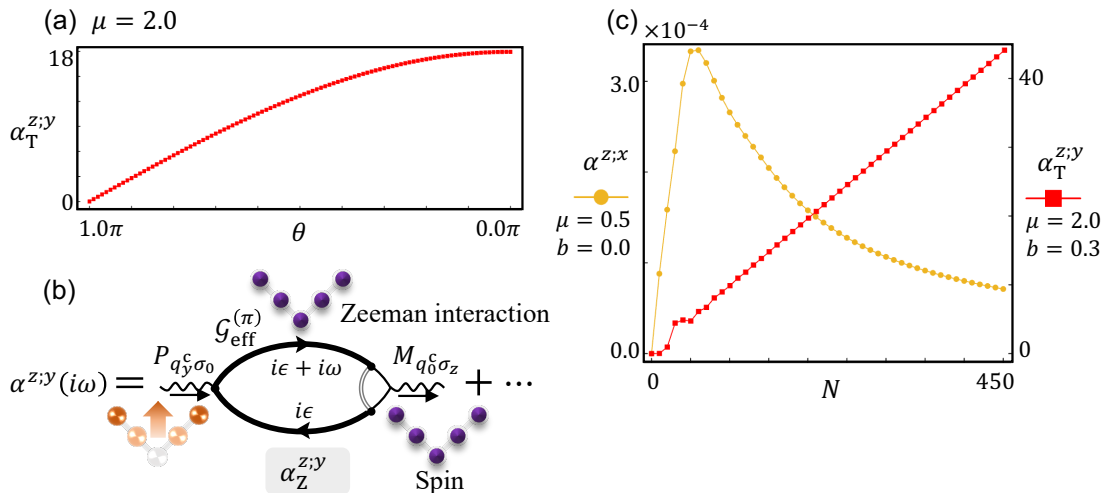


FIG. 7. (a) Apex angle θ dependence of the isothermal ME tensor $\alpha_T^{z;y}$ at $\mu = 2$ in the ferromagnetic s - p model. We set the Hamiltonian parameters as Eq. (14), and $N = 128$ and $T = 0.01$. The ME response increases monotonically as the apex angle θ decreases. (b) Diagrams for the ME effect in the ferromagnetic V-shaped model. (c) The V-shaped lattice size N dependence of the nonmagnetic-driven ME tensor $\alpha^{z;x}$ ($\mu = 0.5, b = 0$) and the magnetic-driven ME tensor $\alpha_T^{z;y}$ ($\mu = 2, b = 0.3$) at $\theta = \pi/2$. The difference in physical mechanisms results in different size dependence.

which leads to a natural expansion as follows:

$$\alpha_{\text{eff}}^{z;y}(i\omega_m) = \alpha_Z^{z;y} + O(\Delta_p^{-1}). \quad (44)$$

$\alpha_T^{z;y}$ and $\alpha_{\text{eff}}^{z;y}(i\omega_m)$ are related by Eq. (23). The corresponding diagram is shown in Fig. 7(b), and its explicit expressions are provided in Appendix C. The diagram in Fig. 7(b) displays that $\alpha_T^{z;y}$ originates from the spin magnetization induced by the coupling between the charge-potential gradient along the y direction generated by the applied electric field and the Zeeman interaction. Its θ dependence is given by

$$\alpha_Z^{z;y} \propto \cos \frac{\theta}{2}. \quad (45)$$

Accordingly, the angular dependence obtained in Fig. 7(a) can be understood as a result of the increased gain of the charge-potential gradient along the y direction when the apex angle becomes sharper.

In addition, the difference in physical mechanisms between the magnetic- and nonmagnetic-driven ME responses results in distinct size dependence. Figure 7(c) shows the V-shaped lattice size N dependence of the nonmagnetic-driven ME tensor $\alpha^{z;x}$ and the ferromagnetic-driven ME tensor $\alpha_T^{z;y}$ in the s - p model. The former $\alpha^{z;x}$, originating from local orbital magnetization and effective spin-orbit interaction, decreases with increasing system size. In contrast, the latter $\alpha_T^{z;y}$, which arises from the coupling between the charge-potential gradient and the Zeeman interaction acting over the entire system, increases proportionally with system size. Taking into account that a constant electric field is applied, this calculation of magnetic-driven ME effect demonstrates that the induced magnetization is proportional to the applied voltage along the y direction.

VI. SUMMARY

In summary, we have theoretically investigated the shape dependence of both nonmagnetic- and magnetic-driven ME responses in the noncentrosymmetric V-shaped chain model. First, we evaluated the shape dependence of the nonmagnetic-driven ME effect numerically based on the Kubo formula in a model including s and p orbitals. As a result, the magnitude of the ME effect reaches its maximum at an apex angle of $\theta \approx 0.6\pi$. To clarify the origin of the shape dependence, we subsequently performed a detailed theoretical analysis of the numerical results. We then constructed a low-energy effective Hamiltonian by projecting onto the s -orbital basis. As a result, we found that the polarity induced by the V-shaped geometry manifests as an effective spin-orbit interaction. Furthermore, by analyzing the shape dependence of the Green's function, we clarified that the geometric effect is described by a T -matrix contribution to the Green's function.

Next, we analyzed the selection rules using the multipole basis. It was revealed that the effective spin-orbit interaction and the orbital angular momentum generated by the motion across the apex angle play an essential role in the ME effect. We also found that the term with angle dependence of $\sin \theta \sin \theta/2$, which exhibits a maximum at $\theta = 2 \tan^{-1} \sqrt{2} \approx 0.608\pi$, is dominant.

Finally, we also investigated the V-shaped ferromagnetic model including the Zeeman interaction. We found that the magnetic-driven ME response originates from the spin magnetization induced by the coupling between the charge-potential gradient along the y direction generated by the applied electric field and the Zeeman inter-

action. The difference in physical mechanisms results in distinct shape and size dependence.

Our results not only clarify the shape effects on the ME response in V-shaped systems but also provide a general guideline for understanding mesoscopic multipoles. The effective spin-orbit interaction that emerges in polar geometries can serve as an essential origin of various physical properties. Furthermore, the analysis of geometrical effects based on the T -matrix formalism offers a powerful approach not only for 1D chain systems but also for more general systems with locally broken symmetries. In addition, the mechanism of the ME effect reveals the microscopic influence of meta-material geometry and is also applicable to bulk sys-

tems such as zigzag chain systems, where a variety of odd-parity multipole physics are expected [46, 67–70] (e.g., $\text{CeRu}_2\text{Al}_{10}$ [71, 72], Ce_3TiBi_5 [73, 74], α - $\text{YbAl}_{1-x}\text{Mn}_x\text{B}_4$ [75], and $\text{NdRu}_2\text{Al}_{10}$ [76]).

ACKNOWLEDGMENTS

This research was supported by JST SPRING (Grant No. JPMJSP2119), and by JSPS KAKENHI (Grants Nos. JP22H00101, JP22H01183, JP23H04869, and JP23K03288), and JST CREST (Grant No. JPMJCR23O4), and JST FOREST (Grant No. JPMJFR2366).

Appendix A: Green's function of simple 1D chain

Here, we consider the nonmagnetic case for simplicity. The Hamiltonian matrix

$$\bar{h}^{(\pi)} = \bar{h}_{\text{eff}}(z + \mu/\hbar)|_{\theta=\pi} \quad (\text{A1})$$

can be expressed as $(2N + 1) \times (2N + 1)$ matrix for the $2N + 1$ sites except for the spin degree of freedom:

$$\bar{h}^{(\pi)} = \bar{h}_0 + \bar{h}_{\text{edge}}, \quad (\text{A2})$$

$$\bar{h}_0 = \begin{pmatrix} \varepsilon_0 - t_2 & t_1 & t_2 & 0 & 0 & \dots & 0 & 0 & 0 \\ t_1 & \varepsilon_0 & t_1 & t_2 & 0 & \dots & 0 & 0 & 0 \\ t_2 & t_1 & \varepsilon_0 & t_1 & t_2 & \dots & 0 & 0 & 0 \\ 0 & t_2 & t_1 & \varepsilon_0 & t_1 & \dots & 0 & 0 & 0 \\ 0 & 0 & t_2 & t_1 & \varepsilon_0 & \dots & 0 & 0 & 0 \\ \vdots & \vdots & \vdots & \vdots & \vdots & \ddots & \vdots & \vdots & \vdots \\ 0 & 0 & 0 & 0 & 0 & \dots & \varepsilon_0 & t_1 & t_2 \\ 0 & 0 & 0 & 0 & 0 & \dots & t_1 & \varepsilon_0 & t_1 \\ 0 & 0 & 0 & 0 & 0 & \dots & t_2 & t_1 & \varepsilon_0 - t_2 \end{pmatrix}, \quad \bar{h}_{\text{edge}} = \begin{pmatrix} 2t_2 & 0 & 0 & \dots & 0 & 0 & 0 \\ 0 & 0 & 0 & \dots & 0 & 0 & 0 \\ 0 & 0 & 0 & \dots & 0 & 0 & 0 \\ \vdots & \vdots & \vdots & \ddots & \vdots & \vdots & \vdots \\ 0 & 0 & 0 & \dots & 0 & 0 & 0 \\ 0 & 0 & 0 & \dots & 0 & 0 & 0 \\ 0 & 0 & 0 & \dots & 0 & 0 & 2t_2 \end{pmatrix}, \quad (\text{A3})$$

where

$$\varepsilon_0 = 2u(z + \mu/\hbar), \quad t_1 = -t_{ss\sigma}, \quad t_2 = -u(z + \mu/\hbar). \quad (\text{A4})$$

By diagonalizing \bar{h}_0 , the eigenenergies $E_{k_m}^{(0)}$ and the eigenstates $\psi_{k_m}^{(0)}(R_n^x)$ are obtained as follows:

$$E_{k_m}^{(0)} = \varepsilon_0 + 2t_1 \cos(k_m a) + 2t_2 \cos(2k_m a), \quad (\text{A5a})$$

$$\psi_{k_m}^{(0)}(R_n^x) = \begin{cases} \sqrt{\frac{2a}{L}} \sin(k_m R_n^x) & (m = \text{even}) \\ \sqrt{\frac{2a}{L}} \cos(k_m R_n^x) & (m = \text{odd}) \end{cases} \quad (\text{A5b})$$

where $L = (2N + 2)a$,

$$k_m = \frac{\pi}{L} m \quad (m = 1, 2, \dots, 2N + 1). \quad (\text{A6})$$

Therefore, the Green's function of \bar{h}_0 is given by as follows:

$$[\bar{\mathcal{G}}_0(z)]_{\sigma\sigma'}^{nn'} = \sum_{k_m} \frac{\psi_{k_m}^{(0)}(R_n^x) \psi_{k_m}^{(0)*}(R_{n'})}{\hbar z + \mu - E_{k_m}^{(0)}} [\bar{\sigma}_0]_{\sigma\sigma'}. \quad (\text{A7})$$

Then, the Green's function of $\bar{h}^{(\pi)}$ is obtained from the Dyson equation:

$$\bar{\mathcal{G}}_{\text{eff}}^{(\pi)} = \bar{\mathcal{G}}_0 + \bar{\mathcal{G}}_0 \bar{h}_{\text{edge}} \bar{\mathcal{G}}_{\text{eff}}^{(\pi)}. \quad (\text{A8})$$

Solving this equation, we obtain

$$\bar{\mathcal{G}}_{\text{eff}}^{(\pi)} = \bar{\mathcal{G}}_0 + \bar{\mathcal{G}}_0 \bar{h}_{\text{edge}} \frac{1}{1 - \bar{\mathcal{G}}_0 \bar{h}_{\text{edge}}} \bar{\mathcal{G}}_0. \quad (\text{A9})$$

Appendix B: Matrix representation of multipoles

We show the matrix elements of the multipole operators [17, 18, 20, 64]. The onsite and real bond degrees of freedom are described by electric multipoles \bar{q}^c and \bar{q}^{bn} and the imaginary bond degrees of freedom are described by magnetic toroidal multipoles \bar{t}^{bn} . As an example, for the 7-site basis ($N = 3$), the relevant matrix elements of the multipoles are given as follows:

$$\begin{aligned} \bar{q}_0^c &= \begin{pmatrix} 1 & 0 & 0 & 0 & 0 & 0 & 0 \\ 0 & 1 & 0 & 0 & 0 & 0 & 0 \\ 0 & 0 & 1 & 0 & 0 & 0 & 0 \\ 0 & 0 & 0 & 1 & 0 & 0 & 0 \\ 0 & 0 & 0 & 0 & 1 & 0 & 0 \\ 0 & 0 & 0 & 0 & 0 & 1 & 0 \\ 0 & 0 & 0 & 0 & 0 & 0 & 1 \end{pmatrix}, \quad \bar{q}_0^{\text{b1}} = \begin{pmatrix} 0 & 1 & 0 & 0 & 0 & 0 & 0 \\ 1 & 0 & 1 & 0 & 0 & 0 & 0 \\ 0 & 1 & 0 & 1 & 0 & 0 & 0 \\ 0 & 0 & 1 & 0 & 1 & 0 & 0 \\ 0 & 0 & 0 & 1 & 0 & 1 & 0 \\ 0 & 0 & 0 & 0 & 1 & 0 & 1 \\ 0 & 0 & 0 & 0 & 0 & 1 & 0 \end{pmatrix}, \quad \bar{q}_0^{\text{b2}} = \begin{pmatrix} 0 & 0 & 1 & 0 & 0 & 0 & 0 \\ 0 & 0 & 0 & 1 & 0 & 0 & 0 \\ 1 & 0 & 0 & 0 & 1 & 0 & 0 \\ 0 & 1 & 0 & 0 & 0 & 1 & 0 \\ 0 & 0 & 1 & 0 & 0 & 0 & 1 \\ 0 & 0 & 0 & 1 & 0 & 0 & 0 \\ 0 & 0 & 0 & 0 & 1 & 0 & 0 \end{pmatrix}, \dots, \\ \bar{q}_0^{c'} &= \begin{pmatrix} 0 & 0 & 0 & 0 & 0 & 0 & 0 \\ 0 & 0 & 0 & 0 & 0 & 0 & 0 \\ 0 & 0 & 1 & 0 & 0 & 0 & 0 \\ 0 & 0 & 0 & 0 & 0 & 0 & 0 \\ 0 & 0 & 0 & 0 & 1 & 0 & 0 \\ 0 & 0 & 0 & 0 & 0 & 0 & 0 \\ 0 & 0 & 0 & 0 & 0 & 0 & 0 \end{pmatrix}, \quad \bar{q}_0^{\text{b2}'} = \begin{pmatrix} 0 & 0 & 0 & 0 & 0 & 0 & 0 \\ 0 & 0 & 0 & 0 & 0 & 0 & 0 \\ 0 & 0 & 0 & 0 & 1 & 0 & 0 \\ 0 & 0 & 0 & 0 & 0 & 0 & 0 \\ 0 & 0 & 1 & 0 & 0 & 0 & 0 \\ 0 & 0 & 0 & 0 & 0 & 0 & 0 \\ 0 & 0 & 0 & 0 & 0 & 0 & 0 \end{pmatrix}, \quad \bar{t}_x^{\text{b2}'} = \begin{pmatrix} 0 & 0 & 0 & 0 & 0 & 0 & 0 \\ 0 & 0 & 0 & 0 & 0 & 0 & 0 \\ 0 & 0 & 0 & 0 & -i & 0 & 0 \\ 0 & 0 & 0 & 0 & 0 & 0 & 0 \\ 0 & 0 & 0 & 0 & 0 & 0 & 0 \\ 0 & 0 & i & 0 & 0 & 0 & 0 \\ 0 & 0 & 0 & 0 & 0 & 0 & 0 \end{pmatrix}, \quad (\text{B1}) \\ \bar{q}_x^c &= \begin{pmatrix} -3 & 0 & 0 & 0 & 0 & 0 & 0 \\ 0 & -2 & 0 & 0 & 0 & 0 & 0 \\ 0 & 0 & -1 & 0 & 0 & 0 & 0 \\ 0 & 0 & 0 & 0 & 0 & 0 & 0 \\ 0 & 0 & 0 & 0 & 1 & 0 & 0 \\ 0 & 0 & 0 & 0 & 0 & 2 & 0 \\ 0 & 0 & 0 & 0 & 0 & 0 & 3 \end{pmatrix}, \quad \bar{q}_y^c = \begin{pmatrix} 3 & 0 & 0 & 0 & 0 & 0 & 0 \\ 0 & 2 & 0 & 0 & 0 & 0 & 0 \\ 0 & 0 & 1 & 0 & 0 & 0 & 0 \\ 0 & 0 & 0 & 0 & 0 & 0 & 0 \\ 0 & 0 & 0 & 0 & 1 & 0 & 0 \\ 0 & 0 & 0 & 0 & 0 & 2 & 0 \\ 0 & 0 & 0 & 0 & 0 & 0 & 3 \end{pmatrix}. \end{aligned}$$

We display schematic pictures of the multipole bases \bar{q}_0^c , \bar{q}_0^{b1} , $\bar{q}_0^{\text{b2}'}$, $\bar{t}_x^{\text{b2}'}$, \bar{q}_x^c , \bar{q}_y^c , and $\bar{\sigma}_\nu$ ($\nu = x, y, z$) in Fig. 8.

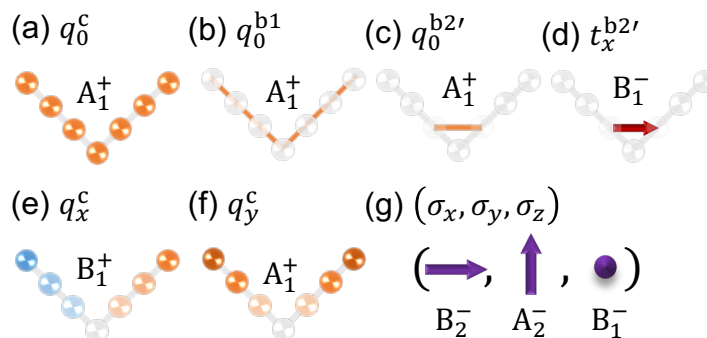


FIG. 8. Schematic pictures of the multipole basis for the cluster, bond, and spin for the 7-site basis, together with the corresponding irreducible representations under the point group C_{2v} . The superscript \pm of the irreducible representation denotes the parity with respect to the time-reversal operation.

Appendix C: Multipole basis representation of the ME tensor

We present the expressions for the ME tensor decomposed in the multipole basis, corresponding to Figs. 5 and 7(b). By separating the θ dependence of each operator in the definition of $\alpha_{\text{eff}}^{z;x}$ in Eq. (24), we obtain the following:

$$\begin{aligned}
\alpha_{\text{eff}}^{z;x}(i\omega_m) &= -\frac{k_B T}{V} \sum_{i\epsilon_n} \text{Tr} \left[\left(\bar{M}_{\text{eff}}^{z(\pi)} + \Delta \bar{M}_{\text{eff}}^{z(\theta)} \right) \left(\bar{\mathcal{G}}^+ + \bar{\mathcal{G}}^+ \bar{\mathcal{T}}^{(\theta)} \bar{\mathcal{G}}^+ \right) \bar{P}^x \left(\bar{\mathcal{G}} + \bar{\mathcal{G}} \bar{\mathcal{T}}^{(\theta)} \bar{\mathcal{G}} \right) \right] \\
&= -\frac{k_B T}{V} \sum_{i\epsilon_n} \text{Tr} \left[\left(M_{q_0^c \sigma_z} (\bar{q}_0^c \bar{\sigma}_z) + M_{q_0^b \sigma_z} (\bar{q}_0^{b2} \bar{\sigma}_z) + \Delta M_{q_0^b \sigma_z} (\bar{q}_0^{b2'} \bar{\sigma}_z) + \Delta M_{t_x^b \sigma_0} (\bar{t}_x^{b2'} \bar{\sigma}_0) \right) \right. \\
&\quad \times \left(\bar{\mathcal{G}}^+ + \bar{\mathcal{G}}^+ [\mathcal{T}_{q_0^c \sigma_0}^+ (\bar{q}_0^c \bar{\sigma}_0) + \mathcal{T}_{q_0^b \sigma_0}^+ (\bar{q}_0^{b2'} \bar{\sigma}_0) + \mathcal{T}_{t_x^b \sigma_0}^+ (\bar{t}_x^{b2'} \bar{\sigma}_z)] \bar{\mathcal{G}}^+ \right) \\
&\quad \times \left. \left(P_{q_x^c \sigma_0} (\bar{q}_x^c \bar{\sigma}_0) \right) \times \left(\bar{\mathcal{G}} + \bar{\mathcal{G}} [\mathcal{T}_{q_0^c \sigma_0} (\bar{q}_0^c \bar{\sigma}_0) + \mathcal{T}_{q_0^b \sigma_0} (\bar{q}_0^{b2'} \bar{\sigma}_0) + \mathcal{T}_{t_x^b \sigma_0} (\bar{t}_x^{b2'} \bar{\sigma}_z)] \bar{\mathcal{G}} \right) \right] \\
&= \alpha_i^{z;x} + \alpha_{\text{ii}}^{z;x} + \alpha_{\text{iii}}^{z;x} + \alpha_{\text{iv}}^{z;x} + O(\Delta_p^{-4}),
\end{aligned} \tag{C1}$$

where $\bar{\mathcal{G}}$ stands for the simple 1D chain Green's function with $\theta = \pi$, the superscript “+” on the Green's function and the T -matrix indicates that their frequency arguments are $i\epsilon_n + i\omega_m$ [e.g., $\bar{\mathcal{G}}^+ = \bar{\mathcal{G}}(i\epsilon_n + i\omega_m)$]. $\mathcal{T}_{q_0^c \sigma_0}$, $\mathcal{T}_{q_0^b \sigma_0}$, $\mathcal{T}_{t_x^b \sigma_z}$, $\Delta M_{q_0^b \sigma_z}$, and $\Delta M_{t_x^b \sigma_0}$ are the components of the T -matrix and the effective magnetization defined in Eqs. (33) and (35). $M_{q_0^c \sigma_z}$, $M_{q_0^b \sigma_z}$, $P_{q_x^c \sigma_0}$, and $P_{q_y^c \sigma_0}$ denote the $\theta = \pi$ components of the effective magnetization and the electric polarization operators along the x and y directions, respectively. Their expressions are given by

$$\begin{aligned}
M_{q_0^c \sigma_z} &= \frac{a}{2V} \text{Tr} \left[(\bar{q}_0^c \bar{\sigma}_z) \bar{M}_{\text{eff}}^{z(\pi)} \right], & M_{q_0^b \sigma_z} &= \frac{a}{2V} \text{Tr} \left[(\bar{q}_0^{b2} \bar{\sigma}_z) \bar{M}_{\text{eff}}^{z(\pi)} \right] \\
P_{q_x^c \sigma_0} &= a \sin \frac{\theta}{2}, & P_{q_y^c \sigma_0} &= a \cos \frac{\theta}{2}.
\end{aligned} \tag{C2}$$

Eq. (44) of $\alpha_{\text{eff}}^{z;y}$ can also be obtained through a similar expansion.

With the condition $\text{Tr}[*] \neq 0$ in mind, and using Eq. (39), $\alpha_i^{z;x}$, $\alpha_{\text{ii}}^{z;x}$, $\alpha_{\text{iii}}^{z;x}$, $\alpha_{\text{iv}}^{z;x}$, and $\alpha_Z^{z;y}$ are given as follows:

$$\alpha_i^{z;x} = -\frac{k_B T}{V} \sum_{i\epsilon_n} \text{Tr} \left[(\bar{t}_x^{b2'} \bar{\sigma}_0) \bar{\mathcal{G}}^+ (\bar{q}_x^c \bar{\sigma}_0) \bar{\mathcal{G}} \right] \Delta M_{t_x^b \sigma_0} P_{q_x^c \sigma_0}, \tag{C3a}$$

$$\begin{aligned}
\alpha_{\text{ii}}^{z;x} &= -\frac{k_B T}{V} \sum_{i\epsilon_n} \text{Tr} \left[(\bar{t}_x^{b2'} \bar{\sigma}_0) \bar{\mathcal{G}}^+ (\bar{q}_x^c \bar{\sigma}_0) \bar{\mathcal{G}} (\bar{q}_0^{b2'} \bar{\sigma}_0) \bar{\mathcal{G}} \right] \Delta M_{t_x^b \sigma_0} P_{q_x^c \sigma_0} \mathcal{T}_{q_0^b \sigma_0} \\
&\quad - \frac{k_B T}{V} \sum_{i\epsilon_n} \text{Tr} \left[(\bar{t}_x^{b2'} \bar{\sigma}_0) \bar{\mathcal{G}}^+ (\bar{q}_0^{b2'} \bar{\sigma}_0) \bar{\mathcal{G}}^+ (\bar{q}_x^c \bar{\sigma}_0) \bar{\mathcal{G}} \right] \Delta M_{t_x^b \sigma_0} \mathcal{T}_{q_0^b \sigma_0}^+ P_{q_x^c \sigma_0},
\end{aligned} \tag{C3b}$$

$$\begin{aligned}
\alpha_{\text{iii}}^{z;x} &= -\frac{k_B T}{V} \sum_{i\epsilon_n} \text{Tr} \left[(\bar{q}_0^c \bar{\sigma}_z) \bar{\mathcal{G}}^+ (\bar{q}_x^c \bar{\sigma}_0) \bar{\mathcal{G}} (\bar{t}_x^{b2'} \bar{\sigma}_z) \bar{\mathcal{G}} \right] M_{q_0^c \sigma_z} P_{q_x^c \sigma_0} \mathcal{T}_{t_x^b \sigma_z} \\
&\quad - \frac{k_B T}{V} \sum_{i\epsilon_n} \text{Tr} \left[(\bar{q}_0^c \bar{\sigma}_z) \bar{\mathcal{G}}^+ (\bar{t}_x^{b2'} \bar{\sigma}_z) \bar{\mathcal{G}}^+ (\bar{q}_x^c \bar{\sigma}_0) \bar{\mathcal{G}} \right] M_{q_0^c \sigma_z} \mathcal{T}_{t_x^b \sigma_z}^+ P_{q_x^c \sigma_0},
\end{aligned} \tag{C3c}$$

$$\begin{aligned}
\alpha_{\text{iv}}^{z;x} &= -\frac{k_B T}{V} \sum_{i\epsilon_n} \text{Tr} \left[(\bar{q}_0^c \bar{\sigma}_0) \bar{\mathcal{G}}^+ (\bar{q}_0^{b2'} \bar{\sigma}_z) \bar{\mathcal{G}}^+ (\bar{q}_x^c \bar{\sigma}_0) \bar{\mathcal{G}} (\bar{t}_x^{b2'} \bar{\sigma}_z) \bar{\mathcal{G}} \right] M_{q_0^c \sigma_z} \mathcal{T}_{q_0^b \sigma_0}^+ P_{q_x^c \sigma_0} \mathcal{T}_{t_x^b \sigma_z} \\
&\quad - \frac{k_B T}{V} \sum_{i\epsilon_n} \text{Tr} \left[(\bar{q}_0^c \bar{\sigma}_0) \bar{\mathcal{G}}^+ (\bar{t}_x^{b2'} \bar{\sigma}_z) \bar{\mathcal{G}}^+ (\bar{q}_x^c \bar{\sigma}_0) \bar{\mathcal{G}} (\bar{q}_0^{b2'} \bar{\sigma}_z) \bar{\mathcal{G}} \right] M_{q_0^c \sigma_z} \mathcal{T}_{t_x^b \sigma_z}^+ P_{q_x^c \sigma_0} \mathcal{T}_{q_0^b \sigma_0},
\end{aligned} \tag{C3d}$$

$$\alpha_Z^{z;y} = -\frac{k_B T}{V} \sum_{i\epsilon_n} \text{Tr} \left[(\bar{q}_0^c \bar{\sigma}_0) \bar{\mathcal{G}}^+ (\bar{q}_y^c \bar{\sigma}_0) \bar{\mathcal{G}} \right] M_{q_0^c \sigma_z} P_{q_y^c \sigma_0}. \tag{C3e}$$

From these equations, the θ and Δ_p dependence of the ME tensor in Eqs. (41) and (45) in the main text is obtained.

- [1] W. Cai, U. K. Chettiar, A. V. Kildishev, and V. M. Shalaev, Optical cloaking with metamaterials, *Nat. Photon.* **1**, 224 (2007).
- [2] C. M. Soukoulis and M. Wegener, Optical metamaterials—more bulky and less lossy, *Science* **330**, 1633 (2010).
- [3] C. M. Soukoulis and M. Wegener, Past achievements and future challenges in the development of three-dimensional photonic metamaterials, *Nat. Photon.* **5**, 523 (2011).
- [4] N. I. Zheludev and Y. S. Kivshar, From metamaterials to metadevices, *Nat. Mater.* **11**, 917 (2012).
- [5] H.-H. Hsiao, C. H. Chu, and D. P. Tsai, Fundamentals and applications of metasurfaces, *Small Methods* **1**, 1600064 (2017).
- [6] M. Matsubara, T. Kobayashi, H. Watanabe, Y. Yanase, S. Iwata, and T. Kato, Polarization-controlled tunable directional spin-driven photocurrents in a magnetic metamaterial with threefold rotational symmetry, *Nat. Commun.* **13**, 6708 (2022).
- [7] M. Hild, L. E. Golub, A. Fuhrmann, M. Otteneder, M. Kroneder, M. Matsubara, T. Kobayashi, D. Oshima, A. Honda, T. Kato, J. Wunderlich, C. Back, and S. D. Ganichev, Terahertz spin ratchet effect in magnetic metamaterials, *Phys. Rev. B* **107**, 155419 (2023).
- [8] M. Kuwata-Gonokami, N. Saito, Y. Ino, M. Kauranen, K. Jefimovs, T. Vallius, J. Turunen, and Y. Svirko, Giant optical activity in quasi-two-dimensional planar nanostructures, *Phys. Rev. Lett.* **95**, 227401 (2005).
- [9] N. Yu, P. Genevet, M. A. Kats, F. Aieta, J.-P. Tetienne, F. Capasso, and Z. Gaburro, Light propagation with phase discontinuities: generalized laws of reflection and refraction, *Science* **334**, 333 (2011).
- [10] J. C. Gartside, A. Vanstone, T. Dion, K. D. Stenning, D. M. Arroo, H. Kurebayashi, and W. R. Branford, Reconfigurable magnonic mode-hybridisation and spectral control in a bicomponent artificial spin ice, *Nat. Commun.* **12**, 2488 (2021).
- [11] D. Sekine, Y. Sato, and M. Matsubara, Nonlinear optical detection of mesoscopic magnetic toroidal dipoles, *Appl. Phys. Lett.* **120**, 162905 (2022).
- [12] S. Hayami and H. Kusunose, Microscopic description of electric and magnetic toroidal multipoles in hybrid orbitals, *J. Phys. Soc. Jpn.* **87**, 033709 (2018).
- [13] S. Hayami, M. Yatsushiro, Y. Yanagi, and H. Kusunose, Classification of atomic-scale multipoles under crystallographic point groups and application to linear response tensors, *Phys. Rev. B* **98**, 165110 (2018).
- [14] H. Watanabe and Y. Yanase, Group-theoretical classification of multipole order: Emergent responses and candidate materials, *Phys. Rev. B* **98**, 245129 (2018).
- [15] M. Yatsushiro, H. Kusunose, and S. Hayami, Multipole classification in 122 magnetic point groups for unified understanding of multiferroic responses and transport phenomena, *Phys. Rev. B* **104**, 054412 (2021).
- [16] H. Kusunose and S. Hayami, Generalization of microscopic multipoles and cross-correlated phenomena by their orderings, *J. Phys.: Condens. Matter* **34**, 464002 (2022).
- [17] R. Oiwa and H. Kusunose, Systematic analysis method for nonlinear response tensors, *J. Phys. Soc. Jpn.* **91**, 014701 (2022).
- [18] S. Hayami and H. Kusunose, Unified description of electronic orderings and cross correlations by complete multipole representation, *J. Phys. Soc. Jpn.* **93**, 072001 (2024).
- [19] H. Kusunose, R. Oiwa, and S. Hayami, Complete multipole basis set for single-centered electron systems, *J. Phys. Soc. Jpn.* **89**, 104704 (2020).
- [20] S. Hayami, Y. Yanagi, and H. Kusunose, Bottom-up design of spin-split and reshaped electronic band structures in antiferromagnets without spin-orbit coupling: Procedure on the basis of augmented multipoles, *Phys. Rev. B* **102**, 144441 (2020).
- [21] X. Gao, X. Han, W.-P. Cao, H. O. Li, H. F. Ma, and T. J. Cui, Ultrawideband and high-efficiency linear polarization converter based on double v-shaped metasurface, *IEEE Trans. Antennas Propag.* **63**, 3522 (2015).
- [22] Y. Xie, C. Yang, Y. Wang, Y. Shen, X. Deng, B. Zhou, and J. Cao, Anomalous refraction and reflection characteristics of bend v-shaped antenna metasurfaces, *Scientific reports* **9**, 6700 (2019).
- [23] J. Hu, S. Bandyopadhyay, Y.-h. Liu, and L.-y. Shao, A review on metasurface: from principle to smart metadevices, *Frontiers in Physics* **8**, 586087 (2021).
- [24] V. Edelstein, Spin polarization of conduction electrons induced by electric current in two-dimensional asymmetric electron systems, *Solid State Commun.* **73**, 233 (1990).
- [25] T. Furukawa, Y. Shimokawa, K. Kobayashi, and T. Itou, Observation of current-induced bulk magnetization in elemental tellurium, *Nat. Commun.* **8**, 954 (2017).
- [26] R. González-Hernández, P. Ritzinger, K. Věborný, J. Železný, and A. Manchon, Non-relativistic torque and edelstein effect in non-collinear magnets, *Nat. Commun.* **15**, 7663 (2024).
- [27] A. Popoola, R. Kashikar, A. Azmy, I. Spanopoulos, H. Jafari, J. Sławińska, S. Witanachchi, S. Lisenkov, and I. Ponomareva, Mechanically and electrically tunable rashba-edelstein effect in ferroelectric semiconductors, CsGeX₃ (X = I, Br, Cl), *Phys. Rev. Mater.* **9**, 084412 (2025).
- [28] I. Sodemann and L. Fu, Quantum nonlinear hall effect induced by berry curvature dipole in time-reversal invariant materials, *Phys. Rev. Lett.* **115**, 216806 (2015).
- [29] L. Xu, M. Yang, S. J. Wang, and Y. P. Feng, Electronic and optical properties of the monolayer group-iv monochalcogenides mx ($m = \text{Ge, Sn}$; $x = \text{S, Se, Te}$), *Phys. Rev. B* **95**, 235434 (2017).
- [30] Q. Ma, S.-Y. Xu, H. Shen, D. MacNeill, V. Fatemi, T.-R. Chang, A. M. Mier Valdivia, S. Wu, Z. Du, C.-H. Hsu, S. Fang, Q. D. Gibson, K. Watanabe, T. Taniguchi, R. J. Cava, E. Kaxiras, H.-Z. Lu, H. Lin, L. Fu, N. Gedik, and P. Jarillo-Herrero, Observation of the nonlinear hall effect under time-reversal-symmetric conditions, *Nature (London)* **565**, 337 (2019).
- [31] H. Wang and X. Qian, Ferroelectric nonlinear anomalous hall effect in few-layer WTe₂, *npj Computational Materials* **5**, 119 (2019).
- [32] M. Nakamura, S. Horiuchi, F. Kagawa, N. Ogawa, T. Kurumaji, Y. Tokura, and M. Kawasaki, Shift current photovoltaic effect in a ferroelectric charge-transfer complex, *Nat. Commun.* **8**, 281 (2017).
- [33] N. Ogawa, M. Sotome, Y. Kaneko, M. Ogino, and Y. Tokura, Shift current in the ferroelectric semiconductor

- tor SbSI, *Phys. Rev. B* **96**, 241203 (2017).
- [34] D. Shin, S. A. Sato, H. Hübener, U. De Giovannini, N. Park, and A. Rubio, Dynamical amplification of electric polarization through nonlinear phononics in 2D SnTe, *npj Computational Materials* **6**, 182 (2020).
- [35] M. S. Okyay, S. A. Sato, K. W. Kim, B. Yan, H. Jin, and N. Park, Second harmonic hall responses of insulators as a probe of berry curvature dipole, *Commun. Phys.* **5**, 303 (2022).
- [36] R. Resta and D. Vanderbilt, Theory of polarization: a modern approach, in *Physics of ferroelectrics: a modern perspective* (Springer, 2007) pp. 31–68.
- [37] C. Cui, F. Xue, W.-J. Hu, and L.-J. Li, Two-dimensional materials with piezoelectric and ferroelectric functionalities, *npj 2D Materials and Applications* **2**, 18 (2018).
- [38] Y. Poplavko, Piezoelectric intrinsic polarity modeling and determination, *APL Materials* **13**, 061113 (2025).
- [39] N. A. Spaldin, M. Fiebig, and M. Mostovoy, The toroidal moment in condensed-matter physics and its relation to the magnetoelectric effect*, *J. Phys.: Condensed Matter* **20**, 434203 (2008).
- [40] Y. V. Kopayev, Toroidal ordering in crystals, *Physics-Uspekhi* **52**, 1111 (2009).
- [41] M. Fiebig, Revival of the magnetoelectric effect, *J. Phys. D: Appl. Phys.* **38**, R123 (2005).
- [42] S. Hayami, H. Kusunose, and Y. Motome, Emergent spin-valley-orbital physics by spontaneous parity breaking, *J. Phys.: Condens. Matter* **28**, 395601 (2016).
- [43] H. Saito, K. Uenishi, N. Miura, C. Tabata, H. Hidaka, T. Yanagisawa, and H. Amitsuka, Evidence of a new current-induced magnetoelectric effect in a toroidal magnetic ordered state of uni4b , *J. Phys. Soc. Jpn.* **87**, 033702 (2018).
- [44] Y. Gao, D. Vanderbilt, and D. Xiao, Microscopic theory of spin toroidization in periodic crystals, *Phys. Rev. B* **97**, 134423 (2018).
- [45] L. Ding, X. Xu, H. O. Jeschke, X. Bai, E. Feng, A. S. Alemany, J. Kim, F.-T. Huang, Q. Zhang, X. Ding, N. Harrison, V. Zapf, D. Khomskii, I. I. Mazin, S.-W. Cheong, and H. Cao, Field-tunable toroidal moment in a chiral-lattice magnet, *Nat. Commun.* **12**, 5339 (2021).
- [46] M. Yatsushiro, R. Oiwa, H. Kusunose, and S. Hayami, Analysis of model-parameter dependences on the second-order nonlinear conductivity in \mathcal{PT} -symmetric collinear antiferromagnetic metals with magnetic toroidal moment on zigzag chains, *Phys. Rev. B* **105**, 155157 (2022).
- [47] A. Kirikoshi and S. Hayami, Finite- q antiferrotoroidal and ferritoroidal order in a distorted kagome structure, *Phys. Rev. B* **111**, L201112 (2025).
- [48] Y. Tokura and N. Nagaosa, Nonreciprocal responses from non-centrosymmetric quantum materials, *Nat. Commun.* **9**, 3740 (2018).
- [49] H. Isobe and N. Nagaosa, Toroidal scattering and nonreciprocal transport by magnetic impurities, *J. Phys. Soc. Jpn.* **91**, 115001 (2022).
- [50] T. Yamanaka, Y. Ihara, and S. Hayami, Nonlinear nonreciprocal electric conductivity driven by magnetic field gradients, *J. Phys. Soc. Jpn.* **94**, 083705 (2025).
- [51] K. Sawada and N. Nagaosa, Optical magnetoelectric effect in multiferroic materials: Evidence for a lorentz force acting on a ray of light, *Phys. Rev. Lett.* **95**, 237402 (2005).
- [52] S. Miyahara and N. Furukawa, Nonreciprocal directional dichroism and toroidal magnons in helical magnets, *J. Phys. Soc. Jpn.* **81**, 023712 (2012).
- [53] J. Mund, D. R. Yakovlev, A. N. Poddubny, R. M. Dubrovinn, M. Bayer, and R. V. Pisarev, Toroidal nonreciprocity of optical second harmonic generation, *Phys. Rev. B* **103**, L180410 (2021).
- [54] J. C. Slater and G. F. Koster, Simplified lcao method for the periodic potential problem, *Phys. Rev.* **94**, 1498 (1954).
- [55] P.-O. Löwdin, Studies in perturbation theory. iv. solution of eigenvalue problem by projection operator formalism, *J. Math. Phys.* **3**, 969 (1962).
- [56] H. Feshbach, Unified theory of nuclear reactions, *Rev. Mod. Phys.* **36**, 1076 (1964).
- [57] J. Leinaas and T. Kuo, Convergence properties of the brillouin-wigner type of perturbation expansion, *Annals of Physics* **111**, 19 (1978).
- [58] N. Hatano and G. Ordonez, Time-reversal symmetric resolution of unity without background integrals in open quantum systems, *J. Math. Phys.* **55**, 122106 (2014).
- [59] A. Altland and B. D. Simons, *Condensed Matter Field Theory*, 2nd ed. (Cambridge University Press, 2010).
- [60] J. Öiké and R. Peters, Impact of electron correlations on the nonlinear edelstein effect, *Phys. Rev. B* **110**, 165111 (2024).
- [61] S. A. Denev, T. T. A. Lummen, E. Barnes, A. Kumar, and V. Gopalan, Probing ferroelectrics using optical second harmonic generation, *J. Am. Ceram. Soc.* **94**, 2699 (2011).
- [62] B. A. Lippmann and J. Schwinger, Variational principles for scattering processes. i, *Phys. Rev.* **79**, 469 (1950).
- [63] J. L. Beeby, Electronic structure of alloys, *Phys. Rev.* **135**, A130 (1964).
- [64] S. Hayami, Y. Yanagi, H. Kusunose, and Y. Motome, Electric Toroidal Quadrupoles in the Spin-Orbit-Coupled Metal $\text{Cd}_2\text{Re}_2\text{O}_7$, *Phys. Rev. Lett.* **122**, 147602 (2019).
- [65] H. Kusunose, R. Oiwa, and S. Hayami, Symmetry-adapted modeling for molecules and crystals, *Phys. Rev. B* **107**, 195118 (2023).
- [66] R. Oiwa, A. Inda, S. Hayami, T. Nomoto, R. Arita, and H. Kusunose, Symmetry-adapted closest wannier modeling based on complete multipole basis set, *Phys. Rev. B* **112**, 035116 (2025).
- [67] Y. Yanase, Magneto-electric effect in three-dimensional coupled zigzag chains, *J. Phys. Soc. Jpn.* **83**, 014703 (2014).
- [68] S. Hayami, H. Kusunose, and Y. Motome, Spontaneous Multipole Ordering by Local Parity Mixing, *J. Phys. Soc. Jpn.* **84**, 064717 (2015).
- [69] S. Hayami, H. Kusunose, and Y. Motome, Asymmetric magnon excitation by spontaneous toroidal ordering, *J. Phys. Soc. Jpn.* **85**, 053705 (2016).
- [70] Y. Suzuki, Tunneling spin current in systems with spin degeneracy, *Phys. Rev. B* **105**, 075201 (2022).
- [71] A. I. Tursina, S. N. Nesterenko, E. V. Murashova, I. V. Chernyshev, H. Noël, and Y. D. Seropegin, $\text{CeRu}_2\text{Al}_{10}$ with the $\text{YbFe}_2\text{Al}_{10}$ structure type, *Acta Crystallographica Section E* **61**, i12 (2005).
- [72] H. Kato, R. Kobayashi, T. Takesaka, T. Nishioka, M. Matsumura, K. Kaneko, and N. Metoki, Magnetic structure determination of $\text{CeT}_2\text{Al}_{10}$ ($T = \text{Ru}$ and Os): Single crystal neutron diffraction studies, *J. Phys. Soc. Jpn.* **80**, 073701 (2011).

- [73] M. Shinozaki, G. Motoyama, T. Mutou, S. Nishigori, A. Yamaguchi, K. Fujiwara, K. Miyoshi, and A. Sumiyama, Study for current-induced magnetization in ferrotoroidal ordered state of Ce_3TiBi_5 , *JPS Conf. Proc.* **30**, 011189 (2020).
- [74] M. Shinozaki, G. Motoyama, M. Tsubouchi, M. Sezaki, J. Gouchi, S. Nishigori, T. Mutou, A. Yamaguchi, K. Fujiwara, K. Miyoshi, and Y. Uwatoko, Magnetoelectric effect in the antiferromagnetic ordered state of ce3tibi5 with ce zig-zag chains, *J. Phys. Soc. Jpn.* **89**, 033703 (2020).
- [75] S. Suzuki, K. Takubo, K. Kuga, W. Higemoto, T. U. Ito, T. Tomita, Y. Shimura, Y. Matsumoto, C. Bareille, H. Wadati, S. Shin, and S. Nakatsuji, High-temperature antiferromagnetism in Yb based heavy fermion systems proximate to a kondo insulator, *Phys. Rev. Res.* **3**, 023140 (2021).
- [76] K. Sudo, Y. Yanagi, M. Araki, H. Tanida, and M. Kimata, Large spontaneous nonreciprocal charge transport in a zero-magnetization antiferromagnet, *arXiv:2511.06009* (2025).